Atmos. Meas. Tech., 13, 2397–2411, 2020
https://doi.org/10.5194/amt-13-2397-2020

Atmospheric Measurement Techniques
Open Access
EGU

Nitrate radical generation via continuous generation of dinitrogen pentoxide in a laminar flow reactor coupled to an oxidation flow reactor

Andrew T. Lambe[1], Ezra C. Wood[2], Jordan E. Krechmer[1], Francesca Majluf[1], Leah R. Williams[1], Philip L. Croteau[1], Manuela Cirtog[3], Anaïs Féron[3], Jean-Eudes Petit[4], Alexandre Albinet[5], Jose L. Jimenez[6], and Zhe Peng[6]

[1]Center for Aerosol and Cloud Chemistry, Aerodyne Research Inc., Billerica, MA, USA
[2]Department of Chemistry, Drexel University, Philadelphia, PA, USA
[3]Laboratoire Inter-Universitaire des Systèmes Atmosphériques (LISA), UMR CNRS 7583, Université Paris-Est-Créteil, Université de Paris, Institut Pierre Simon Laplace (IPSL), Créteil, France
[4]Laboratoire des Sciences du Climat et de l'Environnement (CNRS-CEA-UVSQ), CEA Orme des Merisiers, Gif-sur-Yvette, France
[5]Institut National de l'Environnement Industriel et des Risques (Ineris), Verneuil-en-Halatte, France
[6]Department of Chemistry and Cooperative Institute for Research in Environmental Sciences (CIRES), University of Colorado, Boulder, CO, USA

Correspondence: Andrew T. Lambe (lambe@aerodyne.com) and Zhe Peng (zhe.peng@colorado.edu)

Received: 5 December 2019 – Discussion started: 23 January 2020
Revised: 10 April 2020 – Accepted: 22 April 2020 – Published: 15 May 2020

Abstract. Oxidation flow reactors (OFRs) are an emerging tool for studying the formation and oxidative aging of organic aerosols and other applications. The majority of OFR studies to date have involved the generation of the hydroxyl radical (OH) to mimic daytime oxidative aging processes. In contrast, the use of the nitrate radical (NO_3) in modern OFRs to mimic nighttime oxidative aging processes has been limited due to the complexity of conventional techniques that are used to generate NO_3. Here, we present a new method that uses a laminar flow reactor (LFR) to continuously generate dinitrogen pentoxide (N_2O_5) in the gas phase at room temperature from the NO_2 + O_3 and NO_2 + NO_3 reactions. The N_2O_5 is then injected into a dark Potential Aerosol Mass (PAM) OFR and decomposes to generate NO_3; hereafter, this method is referred to as "OFR-iN_2O_5" (where "i" stands for "injected"). To assess the applicability of the OFR-iN_2O_5 method towards different chemical systems, we present experimental and model characterization of the integrated NO_3 exposure, $NO_3 : O_3$, $NO_2 : NO_3$, and $NO_2 : O_2$ as a function of LFR and OFR conditions. These parameters were used to investigate the fate of representative organic peroxy radicals (RO_2) and aromatic alkyl radicals generated from volatile organic compound (VOC) + NO_3 reactions, and VOCs that are reactive towards both O_3 and NO_3. Finally, we demonstrate the OFR-iN_2O_5 method by generating and characterizing secondary organic aerosol from the β-pinene + NO_3 reaction.

1 Introduction

The importance of nitrate radicals (NO_3) as a nighttime oxidant is well established (Wayne et al., 1991; Brown and Stutz, 2012; Ng et al., 2017). In the atmosphere, $NO_2 + O_3$ is the primary source of NO_3, after which NO_3 exists in equilibrium with NO_2 and N_2O_5. Atmospheric nighttime NO_3 mixing ratios can vary by at least 2 orders of magnitude, ranging from 1 ppt or less in remote areas to 10–400 ppt in polluted urban regions (Finlayson-Pitts and Pitts Jr., 2000; Asaf et al., 2010; Warneck and Williams, 2012; Ng et al., 2017). Atmospheric organic compounds that are reactive towards NO_3 include isoprene and monoterpenes that are emitted from biogenic sources (including urban vegetation), phenols and methoxyphenols emitted from biomass burning, and polycyclic aromatic hydrocarbons (PAHs) emitted from combustion processes. NO_3 oxidation of these compounds

generates oxygenated volatile organic compounds (OVOCs) and/or secondary organic aerosol (SOA), including particulate organic nitrates or nitroaromatics. The importance of these sources and processes are likely to continue to increase for the foreseeable future due to climate change (Melaas et al., 2016; Short, 2017).

Laboratory studies have attempted to elucidate the mechanisms associated with NO_3-initiated oxidative aging processes in the gas and condensed phases and in environmental chambers and flow tubes. Traditional NO_3 generation techniques typically utilize N_2O_5 as the radical precursor. N_2O_5 is generated from the reaction $NO + O_3 \rightarrow NO_2 + O_2$, followed by the reactions $NO_2 + O_3 \rightarrow NO_3 + O_2$ and $NO_2 + NO_3 \rightarrow N_2O_5$. The synthesized N_2O_5 is collected and stored in a cold trap under dry conditions to minimize hydrolysis of N_2O_5 to nitric acid (HNO_3). This method has limitations that hinder widespread usage: specifically, long-term storage and handling of N_2O_5 at low temperature and under dry conditions is difficult, and the continuous generation of N_2O_5 that is required for oxidation flow reactors (OFRs) or other continuous flow chambers is challenging. Thus, field studies investigating the NO_3-induced SOA formation potential of ambient air are extremely limited (Palm et al., 2017). Alternative NO_3 generation techniques that utilize reactions between chlorine atoms and chlorine nitrate ($ClONO_2$) or fluorine atoms and HNO_3 require cold storage of $ClONO_2$ and handling or generation of halogen species that are reactive towards organic compounds (Burrows et al., 1985).

To address issues associated with traditional NO_3 generation techniques, we developed and characterized a new method that is well suited to applications where a continuous source of N_2O_5 and NO_3 is required, such as OFR studies. The method is capable of continuous N_2O_5 generation in the gas phase at room temperature using a laminar flow reactor (LFR) that is coupled to a dark OFR. N_2O_5 injected into the OFR decomposes to generate NO_3 and initiate oxidation of reactive VOCs. Hereafter, we refer to this method as "OFR-iN_2O_5" (where "i" stands for "injected"). We present experimental and model characterization of OFR-iN_2O_5 as a function of LFR and OFR conditions, and we demonstrate the application of OFR-iN_2O_5 to generate and characterize SOA from the β-pinene + NO_3 reaction.

2 Methods

2.1 N_2O_5 and NO_3 generation

Figure 1 shows a process flow diagram of the OFR-iN_2O_5 method. Separate flows containing NO_2 and O_3 were input to a perfluoroalkoxy (PFA) tube with a 2.54 cm o.d. (outer diameter), a 2.22 cm i.d. (inner diameter), and a 152.4 cm length that was operated as an LFR. Previous studies used a similar process to generate N_2O_5 (Wood et al., 2003; Boyd et al., 2015), although the LFR materials, flow rates, and reagent concentrations were different. A compressed gas cylinder containing 1.00 ± 0.02 % NO_2 in N_2 (Praxair) was used to supply NO_2. While not used for this study, replacing NO_2 with NO to avoid NO_2-to-HNO_3 conversion inside the gas cylinder and increasing $[O_3]$ accordingly achieves similar results. O_3 was generated by passing 1750–1800 $cm^3\,min^{-1}$ of pure O_2 through a custom O_3 chamber housing a mercury fluorescent lamp (GPH212T5VH, Light Sources, Inc.) or 500–1800 $cm^3\,min^{-1}$ O_2 through a corona discharge ozone generator (Enaly 1KNT). We used 1800 $cm^3\,min^{-1}$ of O_2 carrier gas flow through the LFR ($Re \sim 110$, i.e., laminar flow) to achieve $\tau_{LFR} = 20$ s for reasons that are discussed in Sect. 3.1. The NO_2 mixing ratio entering the LFR, $[NO_2]_{0,\,LFR}$, was calculated from the NO_2 mixing ratio in the compressed gas mixture and the dilution ratio of 0–50 or 0–1300 $cm^3\,min^{-1}$ gas flow into O_2 which was controlled using mass flow controllers. The O_3 mixing ratio entering the LFR, $[O_3]_{0,\,LFR}$, was measured using a 2B Technologies 106-MFT or a Teledyne M452 flow-through O_3 analyzer when generated from the mercury lamp or corona discharge source, respectively. The output of the LFR was mixed with a carrier gas containing 3.8 L min^{-1} synthetic air and then injected into a Potential Aerosol Mass (PAM) OFR (Aerodyne Research, Inc.), which is a horizontal 13.3 L aluminum cylindrical chamber operated in continuous flow mode (Kang et al., 2007; Lambe et al., 2011, 2019) with 6.5 L min^{-1} flow through the reactor. The mean residence time in the OFR (τ_{OFR}) was 120 ± 34 s ($\pm 1\sigma$), as obtained from measurements of 10 s pulsed inputs of NO_2 to the OFR obtained using a 2B Technologies Model 405 NO_x analyzer (Fig. S1). Across all experiments, the relative humidity in the OFR (RH_{OFR}) was controlled in the range of 7 %–85 % at 23–25 °C by passing the carrier gas through a Nafion humidifier (Perma Pure LLC) or heated recirculating water bath (NESLAB Instruments, Inc.) prior to mixing with the LFR outflow. The O_3 mixing ratio at the exit of the OFR was measured with a 2B Technologies Model 106-M ozone analyzer.

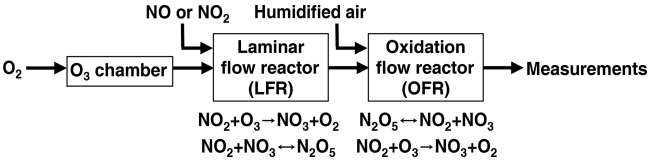

Figure 1. Process flow diagram of the OFR-iN_2O_5 technique used to generate nitrate radicals (NO_3).

2.1.1 OFR-iN_2O_5 characterization studies

In one set of experiments, the integrated NO_3 exposure (NO_{3exp}), defined here as the product of the average NO_3 concentration and τ_{OFR}, was characterized by measuring the decay of VOC tracers reactive towards NO_3 using

a Tofwerk/Aerodyne Vocus proton transfer reaction time-of-flight mass spectrometer (PTR-MS; Krechmer et al., 2018). For this purpose, the tracer decay method is advantageous to direct NO_3 measurements at the OFR inlet and/or outlet, because potential NO_3 concentration gradients inside the OFR that might otherwise bias NO_{3exp} are accounted for. Tracers that were liquid at room temperature were injected into the OFR through a 10.2 cm length of 0.0152 cm i.d. Teflon tubing at a liquid flow rate of about 0.94 µL h^{-1} using a syringe pump, prior to evaporation into a 2.4 L min^{-1} N_2 carrier gas. In preliminary studies, tracers such as isoprene and β-pinene were too reactive towards NO_3 to facilitate accurate characterization of NO_{3exp} over the majority of the OFR-iN_2O_5 conditions that were investigated. Thus, experiments described in this paper used mixtures of tracers with bimolecular k_{NO_3} ranging from approximately 10^{-16} to 10^{-13} cm^3 $molecules^{-1}$ s^{-1} and $k_{O_3} < 10^{-19}$ cm^3 $molecules^{-1}$ s^{-1} (Table S1). Acetonitrile was used as a nonreactive tracer. In "low O_3" experiments ($[O_3]_{0,\,LFR} = 10$ to 300 ppm) a mixture of acetonitrile, butanal, thiophene, 2, 3-dihydrobenzofuran, and naphthalene-d_8 ($C_{10}D_8$), each with mixing ratios of approximately 660, 50, 56, 40, and 18 ppb, respectively, was used. For this tracer mixture, the total external NO_3 reactivity (NO_3R_{ext}), which is the summed product of each tracer mixing ratio and its NO_3 rate constant, was approximately 0.07 s^{-1}. Naphthalene-d_8 was introduced by flowing 5 cm^3 min^{-1} N_2 through a Teflon tube packed with solid $C_{10}D_8$. In "high O_3" experiments ($[O_3]_{0,\,LFR} = 6100$ to 7400 ppm), which generated higher NO_{3exp}, a mixture of acetonitrile (275 ppb), toluene (45 ppb), *o*-xylene (40 ppb), *p*-cymene (31 ppb), 1, 2, 4-trimethylbenzene (35 ppb), 1-butanol (53 ppb), benzaldehyde (47 ppb), butanal (53 ppb), and thiophene (56 ppb) was used, with $NO_3R_{ext} \approx 0.38$ s^{-1}.

In another set of experiments that were conducted as part of the Aerosol Chemical Monitor Calibration Center (ACMCC) particulate organonitrates (*p*ON) experiment (Albinet et al., 2019), direct measurements of NO_3 generated via OFR-iN_2O_5 were performed using a newly developed "incoherent broad band cavity enhanced absorption spectroscopy" (IBBCEAS) technique (Cirtog et al., 2020; Fouqueau et al., 2020). The IBBCEAS instrument that was used measured absorption as a function of wavelength between $\lambda = 640$ and 680 nm, thereby allowing simultaneous measurements of NO_2 and O_3 along with NO_3. During this experiment, *p*ON were generated in a PAM OFR that used $[O_3]_{0,\,LFR} = 150$–160 ppm and $[NO_2]_{0,\,LFR} : [O_3]_{0,\,LFR} = 0.75$, 1.0, and 2.0. IBBCEAS has been used to measure trace NO_3 levels in laboratory and field studies (Venables et al., 2006; Kennedy et al., 2011) utilizing measurement principles that are described in detail by Fiedler et al. (2003) and Langridge et al. (2008). Briefly, measurements were conducted by exciting a high-finesse optical cavity formed by two high reflectivity mirrors with an incoherent broadband source centered on the $\lambda = 662$ nm absorption cross section of NO_3 (2×10^{-17} cm^2, Orphal et al., 2003). Photons resonate between the two mirrors, allowing an effective path length of up to 4.5 km inside the cavity. The absorption coefficient of the sample in the cavity, $\alpha(\lambda)$, was calculated using Eq. (1):

$$\alpha(\lambda) = \left(\frac{I_0(\lambda)}{I(\lambda)} - 1\right)\left(\frac{1 - R(\lambda)}{d}\right) \quad (1)$$

where $\alpha(\lambda)$ is the absorption coefficient of the OFR sample in the instrument, $I(\lambda)$ and $I_0(\lambda)$ were the measured transmitted intensities in the presence and absence of the sample, $d = 61$ cm was the distance between the cavity mirrors, and $R(\lambda)$ was the mirror reflectivity (~ 99.98 %). $I_0(\lambda)$ was obtained by stopping the OFR sample through the instrument and flowing nitrogen from a cylinder (Air Liquide). A period of at least 30 s was allowed between the measurement of $I_0(\lambda)$ and $I(\lambda)$ to ensure the complete purge of the instrument. $R(\lambda)$ was measured before each experiment using a certified calibration cylinder containing 600 ppb NO_2 in zero air (Air Liquide). Concentrations were calculated by applying a least square fit to the measured $\alpha(\lambda)$ considering the absorbing species in the sample:

$$\alpha(\lambda) = [NO_2]\sigma_{NO_2} + [NO_3]\sigma_{NO_3} + [O_3]\sigma_{O_3} + p(\lambda) \quad (2)$$

where NO_2, NO_3, and O_3 are the species absorbing in the spectral region of the instrument, $\alpha(\lambda)$ represents the respective absorption cross sections convoluted with the apparatus function (Vandaele et al., 1998; Voigt et al., 2001; Orphal et al., 2003), and $p(\lambda)$ represents a cubic polynomial to correct baseline deformations due to small LED intensity variations. To avoid saturation of the IBBCEAS in these experiments, the OFR sample was diluted by a controlled dilution factor ranging from 9 to 41, and the detection response was deliberately lowered by reducing the optical path length. The sampling line and optical cavity were made of PFA. The residence time in the IBBCEAS sampling line and instrument ranged from 8.3 to 21.8 s. At these residence times, the calculated transmission efficiencies of NO_3 from the OFR to the IBBCEAS ranged from 0.3 % to 11 %, assuming a NO_3 wall loss rate constant of 0.27 s^{-1} (Kennedy et al., 2011). Corrections to measured NO_3 and NO_2 values accounting for N_2O_5 thermal decomposition and sample dilution were applied to the IBBCEAS results presented in this paper.

To demonstrate the application of OFR-iN_2O_5 to generate SOA, the chemical composition and mass concentration of β-pinene + NO_3 condensed-phase oxidation products was measured with an Aerodyne long-time-of-flight aerosol mass spectrometer (L-ToF-AMS) and/or an aerosol chemical speciation monitor (ACSM). A syringe pump was used to deliver β-pinene (10 %, *v*/*v*, in carbon tetrachloride or 50 %, *v*/*v*, in ethanol) into the carrier gas flow at liquid flow rates ranging from 0.94 to 19 µL h^{-1}. Results presented in this paper assume an AMS or ACSM collection efficiency of 0.5 (Middlebrook et al., 2012) and a relative ionization efficiency of particulate organics equal to 1.6 (Xu et al., 2018).

2.2 Photochemical model

We used the KinSim chemical kinetic solver to calculate concentrations of radical and oxidant species (Peng et al., 2015; Peng and Jimenez, 2017, 2019). The KinSim mechanism shown in Table S2 was adapted from Palm et al. (2017) to model NO_3 and N_2O_5 concentrations in the LFR and OFR. Inputs to the LFR-KinSim model were $[O_3]_{0,\,LFR}$, $[NO_2]_{0,\,LFR}$, RH = 1 %, $T = 24\,^{\circ}C$, $\tau_{LFR} = 20$ s (modeled as plug flow, see Sect. 3.1), and first-order wall loss rates of NO_3 and N_2O_5 ($k_{w_{LFR},\,NO_3}$ and $k_{w_{LFR},\,N_2O_5}$). Inputs to the OFR-KinSim model were $[O_3]$, $[NO_2]$, $[NO_3]$, and $[N_2O_5]$ output from the LFR scaled by a measured dilution factor of 4.4; RH and T measured in the OFR; $\tau_{OFR} = 120$ s, $k_{w_{OFR},\,NO_3}$, and $k_{w_{OFR},\,N_2O_5}$; and input VOC tracer concentrations and their k_{NO_3} values. Because the calculated N_2O_5 residence time in the OFR inlet (~ 0.04 s) was short compared with the N_2O_5 decomposition timescale at $T = 23$–$25\,^{\circ}C$ (~ 20 s), potential thermal decomposition of N_2O_5 during the dilution step was not considered in the model.

2.2.1 LFR and OFR $k_{w,\,NO_3}$ and $k_{w,\,N_2O_5}$ values

Published $k_{w,\,NO_3}$ values onto tubing with a 1 cm (Teflon) and a 4 cm (Pyrex) i.d. are 0.2 and 0.1 s^{-1}, respectively (Dubé et al., 2006; Wood et al., 2003), which bound the 2.22 cm i.d. of the LFR used in this study. Assuming k_w is inversely proportional to the internal diameter of the tube, we assumed $k_{w_{LFR},\,NO_3} = 0.15\,s^{-1}$. Extrapolating this value to the OFR (20.32 cm i.d.) yielded $k_{w_{OFR},\,NO_3} = 0.02\,s^{-1}$. At fixed OFR-i$N_2O_5$ conditions that are summarized in Table S3, varying $k_{w_{LFR},\,NO_3}$ between 0 and 0.3 s^{-1} changed the NO_{3exp} achieved in the OFR by 0.3 %. Results were even less sensitive to the $k_{w_{OFR},\,NO_3}$ assumed for the OFR because of its larger diameter and higher NO_3R_{ext}.

Published $k_{w,\,N_2O_5}$ values onto dry (RH ≈ 20 %) Pyrex or PFA tubing with 4 and 7 cm i.d. are 0.04 and 0.009 s^{-1}, respectively (Wagner et al., 2008; Gržinić et al., 2015). Extrapolating these values to the LFR used here and then averaging them together yielded $k_{w,\,N_2O_5} = 0.05\,s^{-1}$, which was applied in the LFR-KinSim model. In preliminary OFR-KinSim modeling studies, we assumed $k_{w,\,N_2O_5} = 0.014\,s^{-1}$ (Palm et al., 2017). However, as will be discussed in Sect. 3.3, $k_{w,\,N_2O_5}$ was humidity-dependent and required modifications to match measured NO_{3exp} values as a function of RH_{OFR}.

3 Results and discussion

3.1 LFR design considerations

The optimal LFR residence time (τ_{LFR}) was identified using model simulations of the injection of 300 ppm O_3 and NO_2 into the LFR followed by dilution and injection of the LFR output into an OFR operated with $\tau_{OFR} = 120$ s. Figure S2 plots the NO_{3exp} achieved in the OFR as a function of τ_{LFR} ranging from 1 to 60 s. Potential entry length effects that may have influenced results obtained below $\tau_{LFR} \approx 4$–5 s were not considered in the model. Figure S2 shows that the maximum NO_{3exp} in the OFR was obtained at $\tau_{LFR} = 20$ s at room temperature (unheated case); other NO_{3exp} values were normalized to this condition. Below $\tau_{LFR} = 20$ s, NO_{3exp} was suppressed due to higher NO_2 levels entering the OFR. Above $\tau_{LFR} = 20$ s, NO_{3exp} was suppressed due to lower N_2O_5 levels entering the OFR because of more extensive LFR wall loss.

In traditional studies of NO_3 oxidative aging processes that are conducted at low pressure and short residence time ($\tau \sim 1$ s), N_2O_5 is heated to generate a burst of NO_3 prior to injection into the system (Knopf et al., 2011). While not experimentally considered in this work, we modeled the NO_{3exp} achieved assuming complete thermal dissociation of N_2O_5 between the LFR and OFR – for example, by heating to 120 °C for 300 ms (Wood et al., 2003). Figure S2 suggests that the effect of heating N_2O_5 on NO_{3exp} was most significant at short τ_{LFR}, where $[N_2O_5]$ at the exit of the LFR was higher due to less wall loss and room-temperature decomposition. For example, at $\tau_{LFR} = 8$ s, the modeled NO_{3exp} was 2.8 times higher in the complete-dissociation case than in the unheated case, whereas NO_{3exp} increased by factors of 2.3 and 1.5 at $\tau_{LFR} = 20$ and 60 s. Thus, a combination of reducing τ_{LFR} and heating N_2O_5 at the exit of the LFR increases NO_{3exp} and should be explored for future advanced implementations of OFR-iN_2O_5.

3.2 Example OFR-iN_2O_5 characterization studies

Figure 2a shows time series of O_3 and NO_2 concentrations during an OFR-iN_2O_5 characterization experiment where $RH_{OFR} = 11$ %, $[O_3]_{0,\,LFR} = 280$ ppm, and $[NO_2]_{0,\,LFR} =$ 0 to 320 ppm. Figure 2b shows time series of acetonitrile (C_2H_3N), butanal (C_4H_8O), thiophene (C_4H_4S), 2, 3-dihydrobenzofuran (C_8H_8O), and naphthalene-d_8 ($C_{10}D_8$) signals measured during the same period. Following NO_3 generation, the fractional decay of C_2H_3N, C_4H_8O, C_4H_4S, and C_8H_8O increased with increasing tracer k_{NO_3}, as expected. C_8H_8O was too reactive to measure any significant changes in its decay as a function of OFR-iN_2O_5 conditions, as shown in Fig. 2; however, maximum decay of C_4H_8O and C_4H_4S was observed at $[NO_2]_{0,\,LFR} : [O_3]_{0,\,LFR} \approx 0.7$ in this experiment. Decay of naphthalene-d_8, which was influenced by both NO_3 and NO_2 concentrations (Table S1), was maximized at $[NO_2]_{0,\,LFR} : [O_3]_{0,\,LFR} \approx 0.3$ to 1.1.

To confirm that the VOC degradation shown in Fig. 2b was due to reaction with NO_3, Fig. 3 shows IBBCEAS measurements of NO_3 obtained in separate OFR-iN_2O_5 characterization experiments that used $[O_3]_{0,\,LFR} = 150$–160 ppm and $[NO_2]_{0,\,LFR} : [O_3]_{0,\,LFR} = 0.75$ and 2.0. The maximum IBBCEAS signal observed at $\lambda = 662$ nm indicated the presence of NO_3, as is evident from comparison with the

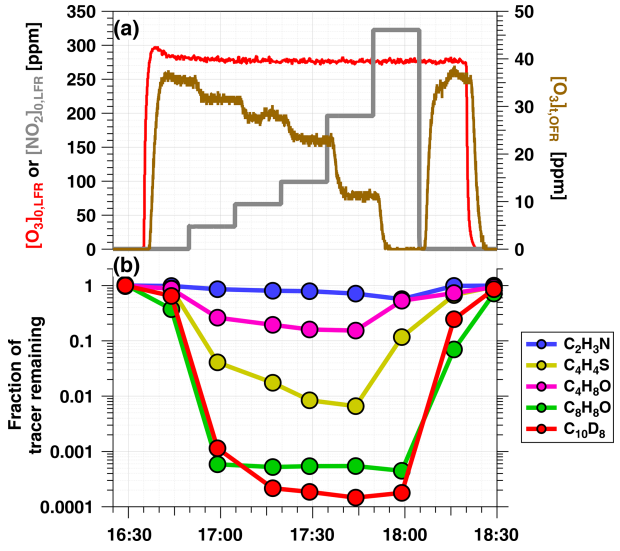

Figure 2. Time series from a representative OFR-iN_2O_5 characterization experiment conducted at $RH_{OFR} = 11\,\%$ of **(a)** O_3 and NO_2 mixing ratios input to LFR (left axis) and O_3 measured at the exit of the OFR (right axis), and **(b)** VOC tracers measured with PTR-MS: acetonitrile (C_2H_3N), butanal (C_4H_8O), thiophene (C_4H_4S), 2, 3-dihydrobenzofuran (C_8H_8O), and naphthalene-d_8 ($C_{10}D_8$).

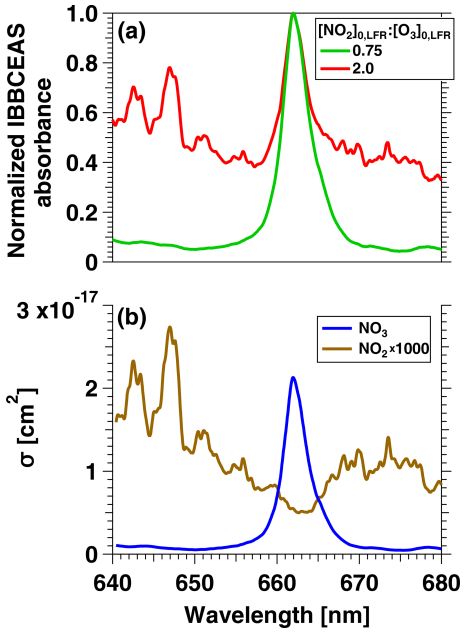

Figure 3. **(a)** IBBCEAS measurements of NO_2 and NO_3 absorbance obtained from an OFR-iN_2O_5 characterization experiment conducted at $[O_3]_{0,\,LFR} = 150$–160 ppm and $[NO_2]_{0,\,LFR}$: $[O_3]_{0,\,LFR} = 0.75$ and 2.0. **(b)** Absorption cross sections of NO_2 and NO_3 (Vandaele et al., 1998; Orphal et al., 2003).

wavelength-dependent absorption cross section of NO_3 obtained by Orphal et al. (2003) and plotted in Fig. 3b. Additionally, Fig. S3 shows the relative rate coefficient obtained from the decay of C_4H_8O and C_4H_4S measured with PTR-MS. We measured a relative rate coefficient of 2.83, which is in agreement with a relative rate coefficient value of 3.22 ± 0.95 calculated from $C_4H_8O + NO_3$ and $C_4H_4S + NO_3$ rate coefficients (Atkinson, 1991; D'Anna et al., 2001). Ions corresponding to peroxy butyl nitrate, nitrothiophene, and nitronaphthalene-d_7, which are known NO_3 oxidation products of C_4H_8O, C_4H_4S, and $C_{10}D_8$, respectively (Atkinson et al., 1990; Jenkin et al., 2003; Saunders et al., 2003; Cabañas et al., 2005), were also detected with PTR-MS. Tracer decay experiments similar to the measurements shown in Fig. 2 were repeated over $[O_3]_{0,\,LFR}$ ranging from 10 to 7400 ppm, $[NO_2]_{0,\,LFR}$ ranging from 0 to 7200 ppm, and RH_{OFR} ranging from 7 % to 85 %. For experiments where $[O_3]_{0,\,LFR} > 6000$ ppm, NO_{3exp} was calculated from the decay of *o*-xylene because (1) *p*-cymene has a large ionized fragment at $C_7H_9^+$ (thus interfering with detection of toluene), (2) NO_3 oxidation products were generated that interfered with detection of oxygenated tracers (butanol, benzaldehyde, and butanal), and (3) the remaining tracers that were used were too reactive towards NO_3 to accurately constrain NO_{3exp}.

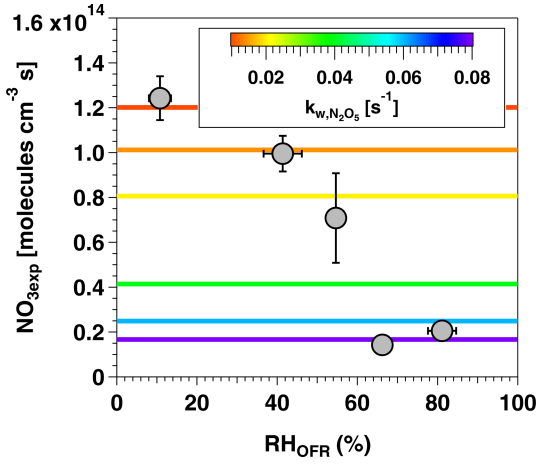

Figure 4. NO_{3exp} as a function of RH_{OFR} at $[O_3]_{0,\,LFR} = 250$ ppm and $[NO_2]_{0,\,LFR} = 130$ ppm. Horizontal lines represent N_2O_5 wall loss rate constants ranging from 0.01 to 0.08 s^{-1} that were input to the OFR-iN_2O_5 KinSim mechanism (Table S2).

3.3 Effect of RH_{OFR}, $[O_3]_{0,\,LFR}$, and $[NO_2]_{0,\,LFR}$ on NO_{3exp}

Figure 4 shows NO_{3exp} as a function of RH_{OFR} at $[O_3]_{0,\,LFR} = 250$ ppm and $[NO_2]_{0,\,LFR} = 130$ ppm. Under these conditions, NO_{3exp} decreased from 1.2×10^{14} to 2.0×10^{13} molecules cm^{-3} s as RH_{OFR} increased from 11 % to 81 %. We hypothesize that this result is due to more effi-

cient hydrolysis of N_2O_5 to HNO_3 on the wetted walls of the OFR at higher RH, thereby suppressing NO_{3exp} relative to values obtained at lower RH conditions. In an attempt to model this behavior, k_{w,N_2O_5} values input to the model were adjusted as a function of RH_{OFR}. Figure 4 suggests that humidity-dependent k_{w,N_2O_5} values ranging from 0.01 to 0.08 s^{-1} were required to cover the range of measured NO_{3exp} . These values agreed within a factor of 2 or better with humidity-dependent k_{w,N_2O_5} values ranging from 0.014 to 0.040 s^{-1} measured by Palm et al. (2017) in a similar OFR and were applied in subsequent model calculations.

Figure 5 shows NO_{3exp} as a function of $[O_3]_{0,LFR}$ for measurements with $[NO_2]_{0,LFR} : [O_3]_{0,LFR} = 0.5 \pm 0.1$ and $RH_{OFR} = 11 \pm 2\,\%$. The equivalent ambient photochemical age shown on the right y axis was calculated assuming a 14 h average nighttime NO_3 mixing ratio of 30 ppt and a 10 h daytime NO_3 mixing ratio of 0 ppt (Asaf et al., 2010). NO_{3exp} increased with increasing $[O_3]_{0,LFR}$ due to increased NO_3 production from higher $[N_2O_5]$. Over the range of measured conditions, increasing $[O_3]_{0,LFR}$ from 33 to 7092 ppm increased NO_{3exp} from 6.4×10^{12} to 4.0×10^{15} molecules cm^{-3} s^{-1}. The black line in Fig. 5 represents NO_{3exp} modeled using the mechanism shown in Table S2. Measured and modeled NO_{3exp} values agreed within a factor of 2 or better above $[O_3]_{0,LFR} \approx 40$ ppm, and the gain in NO_{3exp} as a function of $[O_3]_{0,LFR}$ was highest between $[O_3]_{0,LFR} \approx 10$ and 300 ppm. Over this range of $[O_3]_{0,LFR}$, the NO_2 oxidation lifetime with respect to O_3 decreased from 115 to 4 s. Because $\tau_{LFR} = 20$ s, under this range of LFR conditions, the NO_2 lifetime in the LFR was long enough that high NO_2 levels exiting the LFR suppressed NO_{3exp} in the OFR. In contrast, increasing $[O_3]_{0,LFR}$ from 300 to 7000 ppm decreased the NO_2 oxidation lifetime with respect to O_3 from 4 to 0.2 s, and $[NO_2]$ exiting the LFR was too low to significantly affect NO_{3exp}. To support this hypothesis, Fig. 6 plots NO_{3exp} as a function of $[NO_2]_{0,LFR} : [O_3]_{0,LFR}$ at $[O_3]_{0,LFR} = 250 \pm 20$ ppm and 6850 ± 400 ppm. Here, we incorporated NO_{3exp} values obtained over $RH_{OFR} = 11\,\%$ to 81 % for better statistics, and normalized each NO_{3exp} value to the maximum NO_{3exp} obtained at the same RH. Figure 6 shows that at $[O_3]_{0,LFR} = 250$ ppm, the maximum $NO_{3,exp}$ was achieved at $[NO_2]_{0,LFR} : [O_3]_{0,LFR} \approx 0.5$ to 0.7. Conversely, at $[O_3]_{0,LFR} = 6850$ ppm, the maximum NO_{3exp} value was achieved at $[NO_2]_{0,LFR} : [O_3]_{0,LFR} \approx 1.2$.

In a related set of experiments, IBBCEAS measurements of the $NO_2 : NO_3$ ratio at the exit of the OFR (obtained from Fig. 3a spectra) confirmed that significantly higher NO_2 levels were present in the OFR at higher $[NO_2]_{0,LFR} : [O_3]_{0,LFR}$, as expected. For example, at $[O_3]_{0,LFR} = 150$ ppm and $[NO_2]_{0,LFR} = 112$ ppm, $NO_2 : NO_3 = 28$, whereas at $[O_3]_{0,LFR} = 160$ ppm and $[NO_2]_{0,LFR} = 320$ ppm, $NO_2 : NO_3 = 613$. $NO_2 : NO_3$, along with $NO_3 : O_3$ and $NO_2 : NO_3$, has important implications for the fate of organic species in OFR-iN_2O_5 that are discussed in the following sections.

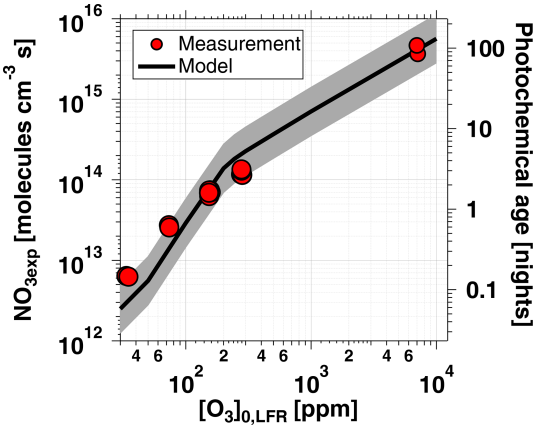

Figure 5. NO_{3exp} as a function of $[O_3]_{0,LFR}$ for measurements with $[NO_2]_{0,LFR} : [O_3]_{0,LFR} = 0.5 \pm 0.1$. Equivalent ambient photochemical age was calculated assuming a 14 h average nighttime NO_3 mixing ratio of 30 ppt and 10 h daytime average NO_3 mixing ratio of 0 ppt (Asaf et al., 2010). Model inputs were $k_{w,N_2O_5} = 0.01\ s^{-1}$ and $NO_3R_{ext} = 0.07\ s^{-1}$ ($[O_3]_{0,LFR} <$ 1000 ppm) or $0.38\ s^{-1}$ ($[O_3]_{0,LFR} > 1000$ ppm). The shaded region encompasses model output scaled by factors of 0.5 and 2.

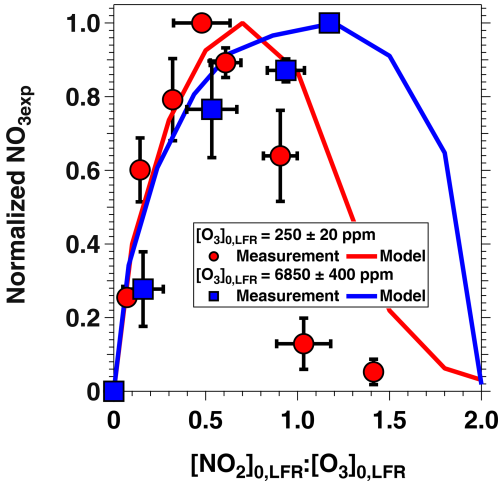

Figure 6. NO_{3exp} as a function of $[NO_2]0,LFR : [O_3]_{0,LFR}$ at fixed $[O_3]_{0,LFR}$ values of 250 ± 20 and 6850 ± 400 ppm and $RH_{OFR} = 11\,\%$ to 81 %. NO_{3exp} values were normalized to the maximum NO_{3exp} value obtained at the same RH.

3.4 Model characterization of OFR-iN_2O_5 : NO_3 : O_3, NO_2 : NO_3, and NO_2 : O_2

To examine OFR-iN_2O_5 performance over a wider range of conditions, Fig. 7 plots the mean NO_{3exp}, $[O_3]$, $NO_3 : O_3$, $NO_2 : NO_3$, and $NO_2 : O_2$ values obtained with the model as a function of $[O_3]_{0,LFR} = 10$ to 10^5 ppm (10 %), for $[NO_2]_{0,LFR} : [O_3]_{0,LFR} = 0.01$, 0.1, 0.5, 1.0, 1.5, 1.8, and 2.0. Three observations are apparent from Fig. 7. First, at $[O_3]_{0,LFR} < 1000$ ppm and $[NO_2]_{0,LFR} : [O_3]_{0,LFR} = 0.01$

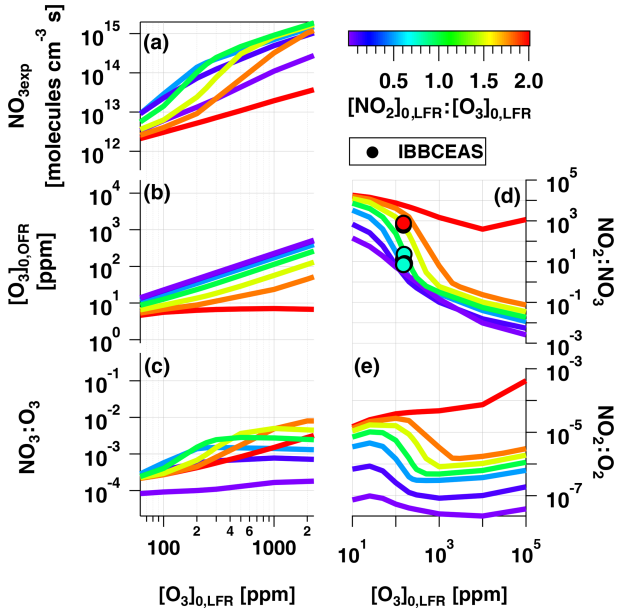

Figure 7. Modeled **(a)** NO_{3exp}, **(b)** $[O_3]$, **(c)** $NO_3 : O_3$, **(d)** $NO_2 : NO_3$, and **(e)** $NO_2 : O_2$ as a function of $[O_3]_{0,\,LFR} = 10$ to 10^5 ppm, for $[NO_2]_{0,\,LFR} : [O_3]_{0,\,LFR} = 0.01$, 0.1, 0.5, 1.0, 1.5, 1.8, and 2.0. Model inputs were $k_{w,\,N_2O_5} = 0.01\,s^{-1}$, $NO_3R_{ext} = 0.07\,s^{-1}$. IBBCEAS-measured $NO_2 : NO_3$ values are plotted in **(d)**.

to 1.8, the maximum NO_{3exp} increased with $[NO_2]_{0,\,LFR} : [O_3]_{0,\,LFR}$ prior to decreasing at $[NO_2]_{0,\,LFR} : [O_3]_{0,\,LFR} > 1.0$ (Fig. 7a). Above $[O_3]_{0,\,LFR} \approx 2000$ ppm and below $[NO_2]_{0,\,LFR} : [O_3]_{0,\,LFR} = 2.0$, NO_{3exp} was less sensitive to $[NO_2]_{0,\,LFR} : [O_3]_{0,\,LFR}$. Second, the maximum $NO_3 : O_3$ increased with increasing $[NO_2]_{0,\,LFR} : [O_3]_{0,\,LFR}$ above $[O_3]_{0,\,LFR} = 1000$ ppm (Fig. 7c). Third, the $[NO_2]_{0,\,LFR} : [O_3]_{0,\,LFR} = 2.0$ case demonstrated unique behavior relative to the other cases because residual O_3 exiting the LFR was low (< 10 ppm) due to almost complete conversion of O_3 to O_2 inside the LFR (Fig. 7b). Consequently, the high residual $[NO_2]$ suppressed NO_{3exp} by 1 to 2 orders of magnitude relative to $[NO_2]_{0,\,LFR} : [O_3]_{0,\,LFR} < 2$ cases (Fig. 7a) and generated enhanced $NO_3 : O_3$, $NO_2 : NO_3$, and $NO_2 : O_2$ values. In addition, $NO_2 : NO_3$ ratios obtained from IBBCEAS measurements at $[O_3]_{0,\,LFR} = 150$ to 160 ppm and $[NO_2]_{0,\,LFR} : [O_3]_{0,\,LFR} = 0.75$, 1.0 and 2.0 are shown in Fig. 7d. The measured $NO_2 : NO_3$ values are comparable to, or lower than, the modeled $NO_2 : NO_3$ values obtained under similar conditions and, therefore, broadly support using model results to further investigate the fate of (1) RO_2 formed from NO_3 oxidation of VOCs, (2) alkyl radicals that are reactive towards NO_2 and O_2, and (3) VOCs that are reactive towards O_3 and NO_3 in the following sections.

3.4.1 Fate of organic peroxy radicals (RO_2) formed from NO_3 + VOC reactions

Organic peroxy radicals (RO_2) react with NO, NO_2, NO_3, HO_2, or other RO_2 to generate alkoxy (RO) radicals, peroxynitrates (RO_2NO_2), hydroperoxides or organic peroxides, and may additionally undergo autooxidation via sequential isomerization and O_2 addition. To investigate the fate of RO_2 as a function of OFR-iN_2O_5 conditions, we applied the methodology of Peng et al. (2019) by calculating the fractional oxidative loss of a generic alkyl or acyl RO_2 to each of these species over the range of conditions shown in Fig. 7. Kinetic data from Orlando and Tyndall (2012) that were used in these calculations are summarized in Table S4. Under almost all OFR-iN_2O_5 conditions shown in Fig. 7, RO_2 reactions with NO, HO_2, and RO_2 were minor (< 1 %) loss pathways compared with reaction with NO_2 and NO_3. We conducted a model sensitivity analysis in which the $RO_2 + RO_2$ reaction rate was enhanced by increasing $NO_3\,R_{ext}$ from 0.07 to $0.7\,s^{-1}$ and increasing the $RO_2 + RO_2$ rate constant from 1×10^{-11} to 1×10^{-10} cm^3 molecule^{-1} s^{-1} (Berndt et al., 2018a, b). Despite these perturbations, the relative contribution of RO_2+RO_2 reactions to total RO_2 loss remained < 1 % across this range of OFR-iN_2O_5 conditions.

To investigate the relative importance of competing RO_2 + NO_2 and $RO_2 + NO_3$ pathways, we defined the fractional reactive loss of RO_2 due to NO_3, $F_{RO_2+NO_3}$:

$$F_{RO_2+NO_3} = \frac{k_{RO_2+NO_3}[NO_3]}{k_{RO_2+NO_3}[NO_3] + k_{RO_2+NO_2}[NO_2]} \quad (3)$$

Figure 8a and b show $F_{RO_2+NO_3}$ calculated for alkyl and acyl RO_2, respectively. To simplify the analysis, we assumed that the thermal decomposition of RO_2NO_2 species formed from $RO_2 + NO_2$ reactions was slow compared with τ_{OFR}. This assumption generates a lower limit $F_{RO_2+NO_3}$ value for the alkyl RO_2 case, where RO_2NO_2 decomposition occurs on timescales of seconds or less (Orlando and Tyndall, 2012) but has minimal influence on the acyl-RO_2 case due to higher thermal stability of peroxyl acyl nitrates. For alkyl RO_2, Fig. 8a shows that $F_{RO_2+NO_3} = 0.5$ was achieved between $[NO_2,\ O_3]_{0,\,LFR} = (125$ ppm, 250 ppm) and (3240 ppm, 1800 ppm). For acyl RO_2, due to faster reaction with NO_2, Fig. 8b shows that $F_{RO_2+NO_3} = 0.5$ was achieved using $[NO_2,\ O_3]_{0,\,LFR} = (350$ ppm, 700 ppm) to (1.1 %, 0.6 %).

To investigate the feasibility of generating OFR-iN_2O_5 conditions where RO_2 loss is dominated by autooxidation, we calculated the lifetime of alkyl and acyl RO_2 (τ_{RO_2}) over the range of OFR-iN_2O_5 conditions shown in Fig. 7 and Fig. 8a and b. As shown in Fig. 8d and e, maximum τ_{RO_2} values of ≈ 1.4 s (alkyl) and 0.4 s (acyl) were obtained at $[NO_2]_{0,\,LFR} \approx 2$ ppm and $[O_3]_{0,\,LFR} \approx 200$ ppm. At lower $[O_3]_{0,\,LFR}$, τ_{RO_2} decreased due to a faster $RO_2 + NO_2$ reaction rate, and at higher $[O_3]_{0,\,LFR}$, τ_{RO_2} decreased due to a faster $RO_2 + NO_3$ reaction rate. Because RO_2 autooxidation

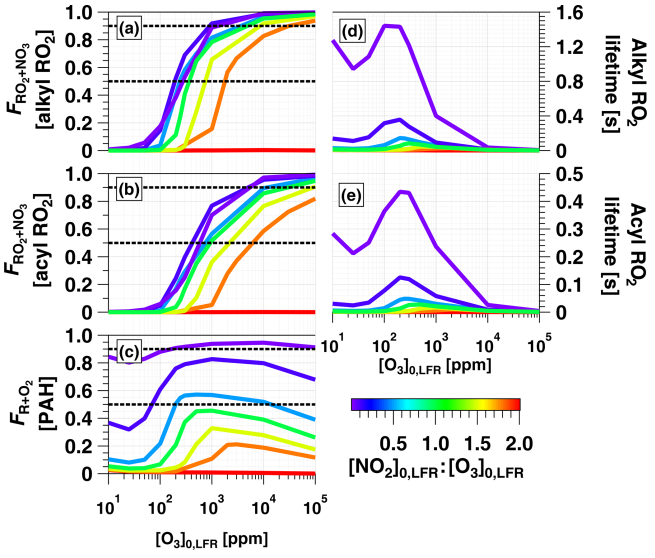

Figure 8. $F_{RO_2+NO_3}$ for **(a)** alkyl and **(b)** acyl RO_2, and **(c)** F_{R+O_2} over the same OFR-iN_2O_5 operating conditions and model inputs used to generate Fig. 7, with the corresponding lifetimes for **(d)** alkyl and **(e)** acyl RO_2.

timescales range from 0.005 to 200 s depending on the specific RO_2 composition (Crounse et al., 2013), OFR-iN_2O_5 may achieve autooxidation-dominant conditions for some RO_2 but not for others.

3.4.2 Fate of aromatic alkyl radicals (R) formed from NO_3 + VOC reactions

The majority of aromatic alkyl radicals (R) that are generated from NO_3 oxidation of VOCs quickly react with O_2 to generate RO_2. However, NO_3 oxidation of a subset of aromatic VOCs generates R that react more slowly with O_2, thereby enabling competing reactions with NO_2. For example, the phenoxy radical (C_6H_5O) generated from NO_3 oxidation of phenol (C_6H_5OH) has $k_{O_2} : k_{NO_2} < 2.4 \times 10^{-9}$ (Platz et al., 1998), and the $C_{10}H_7NO_3$ radical that is generated from NO_3 oxidation of naphthalene ($C_{10}H_8$) has $k_{O_2} : k_{NO_2} < 4 \times 10^{-7}$ (Atkinson et al., 1994). Alkyl radicals generated from NO_3 oxidation of other PAHs may behave similarly to $C_{10}H_7NO_3$, but kinetic data are unavailable in the literature. To investigate the relative importance of competing $R + NO_2$ and $R + O_2$ reactions in these systems, we defined the fractional reactive loss of R with respect to O_2, F_{R+O_2}:

$$F_{R+O_2} = \frac{k_{R+O_2}[O_2]}{k_{R+O_2}[O_2] + k_{R+NO_2}[NO_2]} \quad (4)$$

Figure 8c shows F_{R+O_2} over the same OFR-iN_2O_5 operating conditions used to generate Fig. 7 and Fig. 8a and b. For C_6H_5O (not shown), $F_{R+O_2} < 0.08$ over the entire range of OFR-iN_2O_5 conditions shown in Figs. 7e and 8c. For $C_{10}H_7NO_3$, $F_{R+O_2} \geq 0.5$ was achieved for the majority of OFR-iN_2O_5 conditions where $[NO_2]_{0,LFR} : [O_3]_{0,LFR} \leq 0.1$ and also between $[NO_2, O_3]_{0,LFR} = (100\,\text{ppm}, 200\,\text{ppm})$ and $(5000\,\text{ppm}, 10000\,\text{ppm})$. The use of $[NO_2]_{0,LFR} : [O_3]_{0,LFR} \geq 1$ always generated conditions where the reaction rate of $R + NO_2$ exceeded $R + O_2$.

3.4.3 Fate of VOCs reactive towards O_3 and NO_3

We defined the fractional reactive loss of a VOC with respect to NO_3, F_{VOC+NO_3}:

$$F_{VOC+NO_3} = \frac{k_{VOC+NO_3}[NO_3]}{k_{VOC+NO_3}[NO_3] + k_{VOC+O_3}[O_3]} \quad (5)$$

and we established $F_{VOC+NO_3} = 0.9$ as the criterion for NO_3-dominated oxidative loss. Figure 9 plots $NO_3 : O_3$ at which $F_{VOC+NO_3} = 0.9$ for several classes of organic compounds with published k_{NO_3} and k_{O_3} values greater than 10^{-16} and 10^{-19} cm^{-3} molecules^{-1} s^{-1}, respectively. Therefore, this figure excludes compounds such as alkanes and monocyclic aromatics that react slowly with NO_3 and are essentially unreactive towards O_3 ($F_{NO_3} \approx 1$). $NO_3 : O_3$ values that correspond to $[NO_2]_{0,LFR}$ and $[O_3]_{0,LFR} = (2\,\text{ppm}, 200\,\text{ppm})$, $(150\,\text{ppm}, 300\,\text{ppm})$, and $(5400\,\text{ppm}, 3000\,\text{ppm})$ are represented by horizontal bands with upper and lower limit values calculated assuming k_{w,N_2O_5} values of 0.01 and 0.08 s^{-1} (Sect. 3.3). These LFR inputs generated OFR-iN_2O_5 conditions that maximize the RO_2 lifetime and $NO_3 : O_3$ at $[NO_2] : [O_3]_{0,LFR} = 0.5$ and 1.8, respectively (Figs. 7, 8). Figures 7 and 9 as well as kinetic data from the literature suggest that the injection of 2 ppm NO_2 and 200 ppm O_3 into the LFR was sufficient to achieve $F_{VOC+NO_3} \geq 0.9$ for phenols, PAHs with no double bonds, and mono- and sesquiterpenes with one double bond at low RH_{OFR}. Increasing $[NO_2]_{0,LFR}$ to 150 ppm and $[O_3]_{0,LFR}$ to 300 ppm additionally achieved $F_{VOC+NO_3} \geq 0.9$ for acenaphthylene, isoprene, and mono- and sesquiterpenes with one double bond at elevated RH_{OFR}. Further increasing $[NO_2]_{0,LFR}$ to 5400 ppm and $[O_3]_{0,LFR}$ to 3000 ppm achieved $F_{VOC+NO_3} \geq 0.9$ for $\geq$C3 linear alkenes, unsaturated aldehydes, and mono- and sesquiterpenes with two double bonds at low RH_{OFR}. While $[NO_2, O_3] = [20\,\%, 10\,\%]$ (not shown) achieved $F_{VOC+NO_3} \geq 0.9$ for (E)-3-penten-2-one and ethene, the corresponding $NO_{3exp} \approx 10^{14}$ molecules cm^{-3} s achieved at this condition (Fig. 7a) was insufficient to oxidize more than 1 %–2 % of the initial ethene concentration due to its slow NO_3 rate constant (Atkinson, 1991).

3.5 NO_3 estimation equation for OFR-iN_2O_5

Previous studies reported empirical OH exposure algebraic estimation equations for use with OFRs (Li et al., 2015; Peng et al., 2015, 2018; Lambe et al., 2019). These equations parameterize OH_{exp} as a function of readily measured experimental parameters, thereby providing a simpler alternative to detailed photochemical models for experimental planning

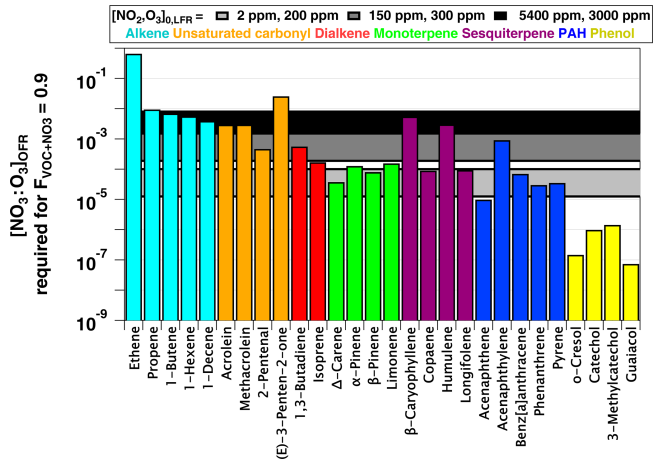

Figure 9. $NO_3 : O_3$ at which $F_{VOC+NO_3} = 0.9$ for representative VOCs with $k_{NO_3} > 10^{-16}$ and $k_{O_3} > 10^{-19}$ cm^3 molecules^{-1} s^{-1} (Manion et al., 2015). Horizontal bands represent upper and lower limit values calculated assuming $k_{w,\,N_2O_5} = 0.01$ and 0.08 s^{-1}.

and analysis. Here, we expand on those studies by deriving an NO_{3exp} estimation equation for OFR-iN_2O_5. Model results obtained from the base case of the model – a VOC reacting with NO_3 at 2.5×10^{-12} cm^3 molecule^{-1} s^{-1} as a surrogate for NO_3R_{ext} – were used to derive the following equation that allows for the estimation of NO_{3exp} for OFR-iN_2O_5:

$$\begin{aligned}\log[(NO_3)_{exp}] = {} & a + b\log[273.15 + T_{OFR}] + c\log[\tau_{OFR}] \\ & + d\log[NO_2]_{0,\,LFR} + e\log[O_3]_{0,\,LFR} \cdot T_{OFR} \\ & + f\log[k_{w_{OFR},\,N_2O_5}] + \log\left(\frac{[NO_2]_{0,\,LFR}}{[O_3]_{0,\,LFR}}\right) \\ & \cdot \left(g\,(\log[O_3]_{0,\,LFR})^2 + h\log[O_3]_{0,\,LFR}\right) - \frac{[NO_2]_{0,\,LFR}}{[O_3]_{0,\,LFR}} \\ & \cdot (i + j\log[O_3]_{0,\,LFR}) + k\log(NO_3R)_{ext} \\ & + l\log[NO_2]_{0,\,LFR} \cdot T + m\log[O_3]_{0,\,LFR} \cdot \log k_{w_{OFR},\,N_2O_5}\end{aligned} \quad (6)$$

The phase space of OFR-iN_2O_5 parameters for fitting Eq. (6) to the NO_{3exp} model results was defined as follows: $[O_3]_{0,\,LFR} = 10$–1000 ppm, $[NO_2]_{0,\,LFR} = 10$–1000 ppm, $[NO_2]_{0,\,LFR} : [O_3]_{0,\,LFR} \le 2$, $NO_3R_{ext} = 1$–200 s^{-1}, $k_{w_{OFR},\,N_2O_5} = 0.01$–0.08 s^{-1}, $T_{OFR} = 0$–40 °C, and $\tau_{OFR} = 60$–300 s. The cases where $[O_3]_{0,\,LFR} > 1000$ ppm and/or $[NO_2]_{0,\,LFR} : [O_3]_{0,\,LFR} > 2$ were not considered due to less practical interest. We explored 11, 11, 7, 4, and 5 logarithmically evenly distributed values in the ranges of $[O_3]_{0,\,LFR}$, $[NO_2]_{0,\,LFR}$ (11 values over 10–1000 ppm), NO_3R_{ext}, $k_{w,\,N_2O_5}$, and τ_{OFR}, respectively. Due to significantly different chemical regimes in different parts of the phase space, fit coefficients that are reported in Table 1 were obtained by fitting the same functional form

Table 1. Fit parameters for NO_{3exp} estimation equation (Eq. 6).

Parameter	Subspace 1 values	Subspace 2 values	Subspace 3 values
a	61.0694	−59.3835	246.416
b	−20.1400	27.3434	−122.229
c	0.795209	0.803508	0.581443
d	−0.375825	1.18285	51.2355
e	0.0311034	0.00815681	−0.66569
f	0.888193	−0.0731138	−0.0210958
g	−0.379009	0.13199	−0.346062
h	1.73605	−0.422009	−81.9221
i	0.14737	0.035132	−22.4373
j	0.261402	0.311104	13.204
k	−1.22009	−0.323329	−0.118988
l	0.00733645	−0.004277	0.676436
m	−0.957064	−0.436977	−0.3983

(Eq. 6) over three subphase spaces with the following additional constraints: (1) $[NO_2]_{0,\,LFR} : [O_3]_{0,\,LFR} = 0$–1 and $NO_3R_{ext} = 20$–200 s^{-1}; (2) $[NO_2]_{0,\,LFR} : [O_3]_{0,\,LFR} = 0$–1 and $NO_3R_{ext} = 1$–20 s^{-1}; and (3) $[NO_2]_{0,\,LFR} : [O_3]_{0,\,LFR} = 1$–2. For these three subspaces, 10080, 13440, and 5880 respective model cases were simulated. In Eq. (6), the terms involving the coefficients g–j were included to reproduce the relationship between normalized NO_{3exp} and $[NO_2]_{0,\,LFR} : [O_3]_{0,\,LFR}$ shown in Fig. 5. Logarithms of first- and second-order terms were successively added until no further fit quality improvement was achieved. Figure 10 compares NO_{3exp} estimated from Eq. (6) and calculated from the model described in Sect. 2.2. The mean absolute value of the relative deviation was 49 % which is comparable to results obtained for previous estimation equations with significant NO_y chemistry (Peng et al., 2018).

NO_3R_{ext} of a system will change over the course of multiple generations of NO_3 oxidation due to changes in kinetic rate coefficients between different species and NO_3 (k_{NO_3}). The sensitivity of Eq. (6) to changes in NO_3R_{ext} depends in part on the relative magnitudes of NO_3R_{ext} and the internal NO_3 reactivity, NO_3R_{int}, which is approximately equal to $k_{NO_2+NO_3}[NO_2]$. If $NO_3R_{int} \gg NO_3R_{ext}$, changes in NO_3R_{ext} would have minimal influence on Eq. (6). In one case study, we examined changes in NO_3R_{ext} following conversion of biogenic VOCs (BVOCs) to gas-phase carbonyl oxidation products with known k_{NO_3} values. Table S5 compares k_{NO_3} of isoprene to methyl vinyl ketone and methacrolein, α-pinene to pinonaldehyde, sabinene to sabinaketone, and 3-carene to caronaldehyde. At the limit where 100 % of each BVOC is converted to its carbonyl oxidation product, NO_3R_{ext} decreases by a factor of 200 or greater. Unsaturated organic nitrates that are generated from BVOC + NO_3 may also be reactive towards NO_3, but k_{NO_3} for these species are not available. In another case study, we examined changes in NO_3R_{ext} following conversion of

BVOCs to SOA. An effective k_{NO_3} for SOA was calculated using the following equation adapted from Lambe et al. (2009):

$$k_{NO_3} = \frac{3}{2}\frac{\gamma \times \bar{c} \times M_{SOA} \times F_{diff}}{D_p \times \rho_p \times N_A}, \quad (7)$$

where F_{diff} is a correction factor accounting for diffusion limitations to the particle surface in the transition regime (Fuchs and Sutugin, 1970),

$$F_{diff} = \frac{1 + 6 \times \frac{D_{NO_3}}{\bar{c} \times D_p}}{1 + 10.26 \times \frac{D_{NO_3}}{\bar{c} \times D_p} + 47.88 \times \left(\frac{D_{NO_3}}{\bar{c} \times D_p}\right)^2}; \quad (8)$$

γ is the fraction of collisions between NO_3 and SOA resulting in reaction; D_p is the surface area-weighted mean particle diameter; ρ_p is the particle density; N_A is Avogadro's number; $\bar{c}$ is the mean molecular speed of NO_3 (3.2×10^4 cm s^{-1} at $T = 298$ K); M_{SOA} is the mean molecular weight of the SOA; and $D_{NO_3} = 0.08$ cm^2 s^{-1} is the NO_3 diffusion coefficient in air (Rudich et al., 1996). Figure S4 shows k_{SOA+NO_3} as a function of D_p ranging from 1 to 1000 nm, assuming $\rho_p = 1.4$ g cm^{-3}, $M_{SOA} = 250$ g mol^{-1} (Nah et al., 2016), and an upper limit $\gamma = 0.1$ for BVOC-derived SOA (Ng et al., 2017). For reference, the range of slowest (isoprene) and fastest (humulene) known $k_{BVOC+NO_3}$ are indicated by the vertical blue line on the y axis. At the limit where 100 % of a BVOC is converted to SOA, NO_3R_{ext} decreases by a factor of 10 or greater depending on $k_{BVOC+NO_3}$ and D_p. Taken together, these results suggest that NO_3R_{ext} decreases following NO_3 oxidation of BVOCs to carbonyl oxidation products and/or SOA. In this case, inputting NO_3R_{ext} of the BVOC precursor to Eq. (6) generates a lower limit to NO_{3exp} over multiple generations of NO_3 oxidation. Results for other systems will depend on the k_{NO_3} values of associated gas- and condensed-phase precursors and their oxidation products.

3.6 SOA generation from β-pinene + NO_3

To apply the OFR-iN_2O_5 technique to SOA formation studies, we generated SOA from β-pinene + NO_3 in the absence of seed particles using $[O_3]_{0,\,LFR} = 300$ ppm, $[NO_2]_{0,\,LFR} = 150$ ppm, and $RH_{OFR} \approx 1$ %. PTR-MS measurements confirmed the complete consumption of β-pinene, and numerous product ions were detected. The largest ions detected were $(H^+)C_9H_{14}O$ and $(H^+)C_{10}H_{14}$ which may correspond to nopinone ($C_9H_{14}O$) and fragmentation or decomposition products of $C_{10}H_{17}NO_4$, respectively (Hallquist et al., 1999; Claflin and Ziemann, 2018). The mass yield of SOA ranged from 0.03 to 0.39 over β-pinene mixing ratios ranging from 20 to 400 ppbv that were injected into the OFR. These yield values are broadly consistent with previous environmental chamber studies (Ng et al., 2017) but are lower than chamber SOA yields obtained at the same β-pinene mixing ratio, presumably due to the absence of seed particles in the OFR (Lambe et al., 2015). To compare the results obtained using OFR-iN_2O_5 with a conventional environmental chamber method, Fig. 11a and b show HR-ToF-AMS spectra of SOA generated from NO_3 oxidation of β-pinene in the Georgia Tech chamber (Boyd et al., 2015) and in the OFR, along with a scatter plot of relative ion abundances present in the two spectra (Fig. 11c). The same spectra are presented on a logarithmic scale in Fig. S5. As is evident, β-pinene + NO_3 SOA generated in the chamber and OFR exhibit a high degree of similarity (linear regression slope = 0.98 and $r^2 = 0.99$). The largest ion signal was observed at NO^+, which, along with the signal at NO_2^+ and $NO^+ : NO_2^+ = 6.7$, is consistent with the formation of particulate organic nitrates (Farmer et al., 2010). Signals observed at CHO^+, $C_2H_3O^+$, and other $C_xH_yO^+_{>1}$ ions suggest the presence of other multifunctional oxidation products.

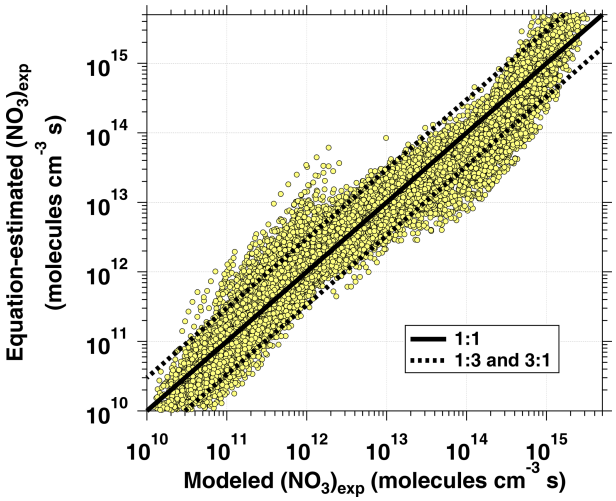

Figure 10. NO_{3exp} calculated from the estimation equation (Eq. 6 and Table 1) as a function of NO_{3exp} calculated from the full OFR-iN_2O_5 KinSim mechanism (Table S2). Solid and dashed lines correspond to the 1 : 1 and the 1 : 3, and 3 : 1 lines, respectively.

4 Conclusions

OFR-iN_2O_5 complements recently developed methods that enable NO_x-dependent photooxidation studies in OFRs such as OFR-iN_2O and OFR-iC_3H_7ONO (Lambe et al., 2017; Peng et al., 2018; Lambe et al., 2019) by enabling studies of nighttime NO_3-initiated oxidative aging processes. Important OFR-iN_2O_5 parameters are $[O_3]$, $[NO_2]$, $[H_2O]$, T, NO_3R_{ext}, and τ_{OFR}. By contrast, important OFR-iN_2O and OFR-iC_3H_7ONO parameters are UV intensity, external OH reactivity (OHR_{ext}), τ_{OFR}, and either $[O_3] + [H_2O] + [N_2O]$ or $[C_3H_7ONO]$. Notably, NO_3R_{ext} is typically less significant in OFR-iN_2O_5 than OHR_{ext} in OFR-iN_2O or OFR-iC_3H_7ONO because (1) most compounds are less reactive

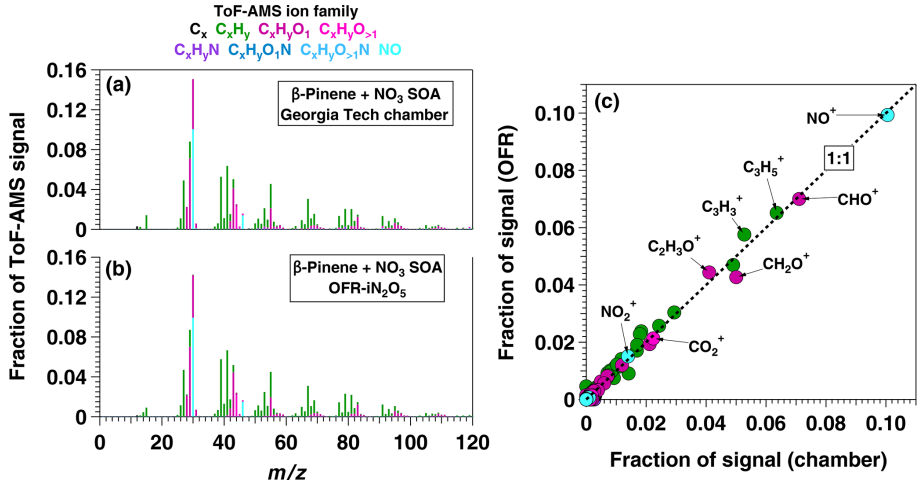

Figure 11. AMS spectra of SOA generated from NO_3 oxidation of β-pinene in **(a)** the Georgia Tech environmental chamber (Boyd et al., 2015) and **(b)** OFR-iN_2O_5. The scatter plot in **(c)** shows spectra generated in the OFR and in the chamber plotted against each other.

towards NO_3 than OH; (2) NO_{3exp} is higher than OH_{exp}; and (3) $(NO_3R)_{int}$ of OFR-iN_2O_5, which is dominated by the $NO_3 + NO_2$ reaction, is larger and easier to manipulate than the internal OH reactivity of OFR-iN_2O and OFR-iC_3H_7ONO, which is dominated by $OH + HO_2$ and $OH + NO_2$ reactions. To identify optimal OFR-iN_2O_5 conditions for different applications, we characterized NO_{3exp}, τ_{RO_2}, $F_{RO_2+NO_3}$, F_{R+O_2}, and F_{VOC+NO_3} at $[O_3]_{0,\,LFR} = 10$ ppm to 10 %, $[NO_2]_{0,\,LFR} : [O_3]_{0,\,LFR} = 0.01$ to 2.0, and $RH_{OFR} =$ 7 % to 85 %. Optimal NO_{3exp} was achieved by minimizing $[H_2O]$ in the OFR and associated humidity-dependent N_2O_5 wall losses. This is contrary to most OFR techniques that are used to generate OH radicals, where optimal OH_{exp} is achieved by maximizing $[H_2O]$ and the associated OH production from the $O(^1D) + H_2O$ reaction and/or H_2O photolysis at $\lambda = 185$ nm.

Figure 12 presents image plots that represent OFR-iN_2O_5 conditions suitable for generating optimal NO_{3exp}, $NO_3 : O_3$, $NO_2 : NO_3$, and τ_{RO_2} values at the lower and upper limit $k_{w,\,N_2O_5}$ values that were measured. Most OFR-iN_2O_5 conditions using $[O_3]_{0,\,LFR} > 200$ ppm generated $NO_{3exp} > 1.5 \times 10^{12}$ molecules cm^{-3} s (Fig. 12a, b), which is sufficient to oxidize isoprene and compounds with similar k_{NO_3}; for reference, $NO_{3exp} > 1.6 \times 10^{11}$ molecules cm^{-3} s is required to oxidize α-pinene. At $[O_3]_{0,\,LFR} > 200$ ppm and $[NO_2]_{0,\,LFR} : [O_3]_{0,\,LFR} > 0.5$, OFR-i$N_2O_5$ generated $NO_3 : O_3 > 10^{-3}$ at $k_{w,\,N_2O_5} = 0.01\ s^{-1}$ (Fig. 12c), which achieved $F_{VOC+NO_3} >$ 0.9 for mono- and sesquiterpenes with one double bond, most PAHs, and phenol/methoxyphenol species. Achieving $NO_3 : O_3 > 10^{-3}$ at $k_{w,\,N_2O_5} = 0.08\ s^{-1}$ was more challenging (Fig. 12d). Increasing $[O_3]_{0,\,LFR}$ decreased $[NO_2] : [NO_3]$ and, therefore, increased $F_{RO_2+NO_3}$ (Fig. 12e, f). In contrast, decreasing $[O_3]_{0,\,LFR}$ or increasing $k_{w,\,N_2O_5}$, and, consequently, NO_{3exp}, increased τ_{RO_2} (Fig. 12g, h), potentially allowing more time for the autooxidation processes

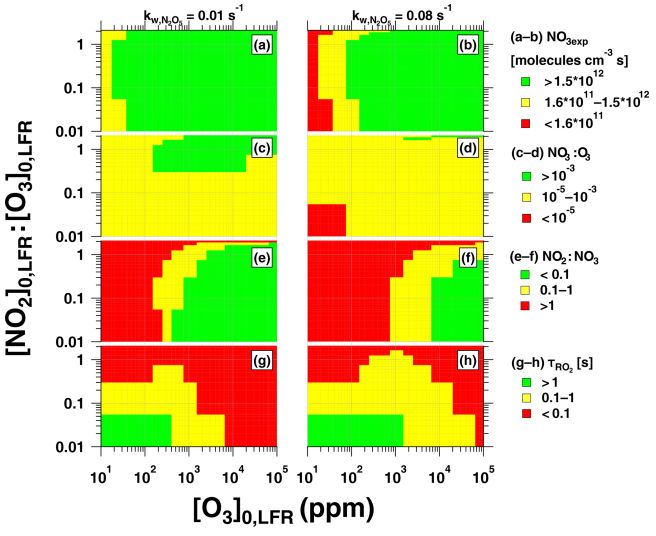

Figure 12. Summary of OFR-iN_2O_5 operating conditions suitable for maximum **(a, b)** NO_3exp, **(c, d)** $NO_3 : O_3$, **(e, f)** $NO_2 : NO_3$, and **(g, h)** τ_{RO_2}, assuming $k_{w,\,N_2O_5} = 0.01$ and $0.08\ s^{-1}$.

to occur. The best overlap between OFR-iN_2O_5 conditions that achieved $F_{RO_2+NO_3} > 0.9$ and $\tau_{RO_2} > 1$ s was obtained with $[NO_2]_{0,\,LFR} \approx$ 2–3 ppm and $[O_3]_{0,\,LFR} \approx$ 200–300 ppm. Because atmospheric $NO_2 : NO_3$ is highly variable and often much larger than $NO_2 : NO_3$ achieved using OFR-iN_2O_5 (Brown et al., 2003; Stutz et al., 2004), simply attempting to maximize $F_{RO_2+NO_3}$ may not always be necessary and has trade-offs such as decreasing $NO_3 : O_3$ and F_{VOC+NO_3}. OFR-iN_2O_5 was more difficult to apply to species such as unsaturated carbonyls and mono- and sesquiterpenes with multiple double bonds that react more efficiently with O_3 than other VOCs; here, alternative NO_3 generation techniques that do not introduce O_3 to the OFR warrant consideration, even

though they are more difficult to implement (Palm et al., 2017).

Because OFR-iN_2O_5 can continuously generate N_2O_5 and NO_3 at room temperature, it is significantly easier to apply in continuous flow reactor studies than related techniques. However, in addition to the aforementioned considerations, high N_2O_5 and HNO_3 concentrations that are generated using OFR-iN_2O_5 complicate the application of techniques such as iodide-adduct chemical ionization mass spectrometry due to efficient reactions between the iodide reagent ion and N_2O_5 or HNO_3 (Lee et al., 2014). Additionally, the humidity-dependent N_2O_5 wall loss rate must be accurately characterized to model the performance of a specific OFR-iN_2O_5 configuration. Future applications of OFR-iN_2O_5 will investigate the NO_3-initiated OVOC and SOA formation potential of simple and complex precursors in laboratory and field studies.

Code and data availability. Data and KinSim mechanisms presented in this paper are available upon request. The KinSim kinetic solver is freely available at http://tinyurl.com/kinsim-release (Peng and Jimenez, 2020).

Supplement. The supplement related to this article is available online at: https://doi.org/10.5194/amt-13-2397-2020-supplement.

Author contributions. ATL, ECW, and AA conceived and planned the experiments. ATL, JEK, FM, LRW, PLC, AA, and JEP carried out the experiments. MC and AF performed the IBBCEAS measurements and data analysis. AL, JLJ, and ZP conceived and planned the model simulations, and ATL and ZP carried out the model simulations. ATL, ECW, ZP, and JLJ contributed to the interpretation of the results. AL took the lead in writing the paper. All authors provided feedback on the paper.

Competing interests. The authors declare no competing interests.

Acknowledgements. Andrew T. Lambe thanks Christopher Boyd and Sally Ng (Georgia Tech) for sharing AMS data obtained in their environmental chamber, and the following colleagues for helpful discussions: Megan Claflin, Manjula Canagaratna, John Jayne, and Douglas Worsnop from ARI; William Brune from Pennsylvania State University; Manfred Winnewisser from Ohio State University; Karl Christe from the University of Southern California; and Robert Woodward-Massey, Youfeng Wang, and Chunxiang Ye from Peking University. The authors thank the ACMCC and participants of the ACMCC *p*ON experiment in December 2018.

Financial support. The ACMCC *p*ON experiment was supported by the French Ministry of Environment and part of the COST Action CA16109 COLOSSAL and the Aerosol, Clouds, and Trace gases Research InfraStructure (ACTRIS). Zhe Peng and Jose L. Jimenez were supported by the US NSF (grant no. AGS-1822664) and EPA STAR (grant no. 83587701-0). This paper has not been reviewed by the EPA and no endorsement should be inferred.

Review statement. This paper was edited by Keding Lu and reviewed by three anonymous referees.

References

Albinet, A., Petit, J.-E., Lambe, A. T., Kalogridis, A., Heikkinen, L., Graeffe, F., Cirtog, M., Féron, A., Allan, J. D., Bibi, Z., Amodeo, T., Karoski, N., Aujay-Plouzeau, R., Meunier, L., Gros, V., Bonnaire, N., Sarda-Estève, R., Truong, F., Ehn, M., Jokinen, T., Aurela, M., Maasikmets, M., Marin, C., Marmureanu, L., Eriksson, A., Ahlberg, E., Freney, E., Minguillon, M., Croteau, P. L., Jayne, J. T., Williams, L. R., and Favez, O.: Overview of the ACMCC particulate organonitrates (*p*ON) experiment, in: 37th AAAR Conference, 14–18 October 2019, Portland, OR, USA, 2019.

Asaf, D., Tas, E., Pedersen, D., Peleg, M., and Luria, M.: Long-Term Measurements of NO_3 Radical at a Semiarid Urban Site: 2. Seasonal Trends and Loss Mechanisms, Environ. Sci. Technol., 44, 5901–5907, https://doi.org/10.1021/es100967z, 2010.

Atkinson, R.: Kinetics and Mechanisms of the Gas-Phase Reactions of the NO_3 Radical with Organic Compounds, J. Phys. Chem. Ref. Data, 20, 459–507, https://doi.org/10.1063/1.555887, 1991.

Atkinson, R., Arey, J., Zielinska, B., and Aschmann, S. M.: Kinetics and nitro-products of the gas-phase OH and NO_3 radical-initiated reactions of naphthalene-d_8, fluoranthene-d_{10}, and pyrene, Int. J. Chem., 22, 999–1014, https://doi.org/10.1002/kin.550220910, 1990.

Atkinson, R., Tuazon, E. C., Bridier, I., and Arey, J.: Reactions of NO_3-naphthalene adducts with O_2 and NO_2, Int. J. Chem. Kinet., 26, 605–614, https://doi.org/10.1002/kin.550260603, 1994.

Berndt, T., Mentler, B., Scholz, W., Fischer, L., Herrmann, H., Kulmala, M., and Hansel, A.: Accretion Product Formation from Ozonolysis and OH Radical Reaction of α-Pinene: Mechanistic Insight and the Influence of Isoprene and Ethylene, Environ. Sci. Technol., 52, 11069–11077, https://doi.org/10.1021/acs.est.8b02210, 2018a.

Berndt, T., Scholz, W., Mentler, B., Fischer, L., Herrmann, H., Kulmala, M., and Hansel, A.: Accretion Product Formation from Self- and Cross-Reactions of RO_2 Radicals in the Atmosphere, Angew. Chem. Int. Ed., 57, 3820–3824, https://doi.org/10.1002/anie.201710989, 2018b.

Boyd, C. M., Sanchez, J., Xu, L., Eugene, A. J., Nah, T., Tuet, W. Y., Guzman, M. I., and Ng, N. L.: Secondary organic aerosol formation from the β-pinene+NO_3 system: effect of humidity and peroxy radical fate, Atmos. Chem. Phys., 15, 7497–7522, https://doi.org/10.5194/acp-15-7497-2015, 2015.

Brown, S. S. and Stutz, J.: Nighttime radical observations and chemistry, Chem. Soc. Rev., 41, 6405–6447, https://doi.org/10.1039/C2CS35181A, 2012.

Brown, S. S., Stark, H., Ryerson, T. B., Williams, E. J., Nicks Jr., D. K., Trainer, M., Fehsenfeld, F. C., and Ravishankara, A. R.:

Nitrogen oxides in the nocturnal boundary layer: Simultaneous in situ measurements of NO_3, N_2O_5, NO_2, NO, and O_3, J. Geophys. Res., 108, 4299, https://doi.org/10.1029/2002jd002917, 2003.

Burrows, J. P., Tyndall, G. S., and Moortgat, G. K.: Absorption spectrum of NO_3 and kinetics of the reactions of NO_3 with NO_2, Cl, and several stable atmospheric species at 298 K, J. Phys. Chem., 89, 4848–4856, https://doi.org/10.1021/j100268a038, 1985.

Cabañas, B., Baeza, M. T., MartÍn, P., Salgado, S., Villanueva, F., Monedero, E., and Wirtz, K.: Products and Mechanism of the NO_3 Reaction with Thiophene, J. Atmos. Chem., 51, 317–335, https://doi.org/10.1007/s10874-005-3580-5, 2005.

Cirtog, M., Fouqueau, A., Michoud, V., Cazaunau, M., Bergé, A., Maisonneuve, F., Zapf, P., Pangui, E., Landsheere, X., Giacomoni, J., Gobbi, M., Hannotel, L., Paris, A., Roulier, N., Mellouki, A., Formenti, P., Cantrell, C., Doussin, J.-F., and Picquet-Varralut, B.: Development of a Broad Band Cavity Enhanced Absorption Spectrometer for NO_3 measurements on field and first observations of nighttime NO_3 vertical profils over Paris, Atmos. Meas. Tech. Discuss., manuscript in preparation, 2020.

Claflin, M. S. and Ziemann, P. J.: Identification and Quantitation of Aerosol Products of the Reaction of beta-Pinene with NO_3 Radicals and Implications for Gas- and Particle-Phase Reaction Mechanisms, J. Phys. Chem. A, 122, 3640–3652, https://doi.org/10.1021/acs.jpca.8b00692, 2018.

Crounse, J. D., Nielsen, L. B., Jørgensen, S., Kjaergaard, H. G., and Wennberg, P. O.: Autoxidation of Organic Compounds in the Atmosphere, J. Phys. Chem. Lett., 4, 3513–3520, 2013.

D'Anna, B., Andresen, Ø., Gefen, Z., and Nielsen, C. J.: Kinetic study of OH and NO_3 radical reactions with 14 aliphatic aldehydes, Phys. Chem. Chem. Phys., 3, 3057–3063, https://doi.org/10.1039/B103623H, 2001.

Dubé, W. P., Brown, S. S., Osthoff, H. D., Nunley, M. R., Ciciora, S. J., Paris, M. W., McLaughlin, R. J., and Ravishankara, A. R.: Aircraft instrument for simultaneous, in situ measurement of NO_3 and N_2O_5 via pulsed cavity ring-down spectroscopy, Rev. Sci., 77, 34–101, https://doi.org/10.1063/1.2176058, 2006.

Farmer, D. K., Matsunaga, A., Docherty, K. S., Surratt, J. D., Seinfeld, J. H., Ziemann, P. J., and Jimenez, J. L.: Atmospheric Chemistry Special Feature: Response of an aerosol mass spectrometer to organonitrates and organosulfates and implications for atmospheric chemistry, P. Natl. Acad. Sci. USA, 107, 6670–6675, 2010.

Fiedler, S. E., Hese, A., and Ruth, A. A.: Incoherent broad-band cavity-enhanced absorption spectroscopy, Chem. Phys. Lett., 371, 284–294, 2003.

Finlayson-Pitts, B. J. and Pitts Jr., J. N.: Chemistry of the Upper and Lower Atmosphere: Theory, Experiments, and Applications, Academic Press, Cambridge, Massachusetts, US, 2000.

Fouqueau, A., Cirtog, M., Cazaunau, M., Pangui, E., Zapf, P., Siour, G., Landsheere, X., Méjean, G., Romanini, D., and Picquet-Varrault, B.: Implementation of an IBBCEAS technique in an atmospheric simulation chamber for *in situ* NO_3 monitoring: characterization and validation for kinetic studies, Atmos. Meas. Tech. Discuss., https://doi.org/10.5194/amt-2020-103, in review, 2020.

Fuchs, N. A. and Sutugin, A. G.: Highly Dispersed Aerosols, Ann Arbor Science Publishers, Newton, MA, 1970.

Gržinić, G., Bartels-Rausch, T., Berkemeier, T., Türler, A., and Ammann, M.: Viscosity controls humidity dependence of N_2O_5 uptake to citric acid aerosol, Atmos. Chem. Phys., 15, 13615–13625, https://doi.org/10.5194/acp-15-13615-2015, 2015.

Hallquist, M., Wängberg, I., Ljungström, E., Barnes, I., and Becker, K.-H.: Aerosol and Product Yields from NO_3 Radical-Initiated Oxidation of Selected Monoterpenes, Environ. Sci. Technol., 33, 553–559, https://doi.org/10.1021/es980292s, 1999.

Jenkin, M. E., Saunders, S. M., Wagner, V., and Pilling, M. J.: Protocol for the development of the Master Chemical Mechanism, MCM v3 (Part B): tropospheric degradation of aromatic volatile organic compounds, Atmos. Chem. Phys., 3, 181–193, https://doi.org/10.5194/acp-3-181-2003, 2003.

Kang, E., Root, M. J., Toohey, D. W., and Brune, W. H.: Introducing the concept of Potential Aerosol Mass (PAM), Atmos. Chem. Phys., 7, 5727–5744, https://doi.org/10.5194/acp-7-5727-2007, 2007.

Kennedy, O. J., Ouyang, B., Langridge, J. M., Daniels, M. J. S., Bauguitte, S., Freshwater, R., McLeod, M. W., Ironmonger, C., Sendall, J., Norris, O., Nightingale, R., Ball, S. M., and Jones, R. L.: An aircraft based three channel broadband cavity enhanced absorption spectrometer for simultaneous measurements of NO_3, N_2O_5 and NO_2, Atmos. Meas. Tech., 4, 1759–1776, https://doi.org/10.5194/amt-4-1759-2011, 2011.

Knopf, D. A., Forrester, S. M., and Slade, J. H.: Heterogeneous oxidation kinetics of organic biomass burning aerosol surrogates by O_3, NO_2, N_2O_5, and NO_3, Phys. Chem. Chem. Phys., 13, 21050–21062, https://doi.org/10.1039/C1CP22478F, 2011.

Krechmer, J., Lopez-Hilfiker, F., Koss, A., Hutterli, M., Stoermer, C., Deming, B., Kimmel, J., Warneke, C., Holzinger, R., Jayne, J., Worsnop, D., Fuhrer, K., Gonin, M., and de Gouw, J.: Evaluation of a New Reagent-Ion Source and Focusing Ion–Molecule Reactor for Use in Proton-Transfer-Reaction Mass Spectrometry, Anal. Chem., 90, 12011–12018, https://doi.org/10.1021/acs.analchem.8b02641, 2018.

Lambe, A., Miracolo, M., Hennigan, C., Robinson, A., and Donahue, N.: Effective Rate Constants and Uptake Coefficients for the Reactions of Organic Molecular Markers (n-Alkanes, Hopanes, and Steranes) in Motor Oil and Diesel Primary Organic Aerosols with Hydroxyl Radicals, Environ. Sci. Technol., 43, 8794–8800, 2009.

Lambe, A. T., Ahern, A. T., Williams, L. R., Slowik, J. G., Wong, J. P. S., Abbatt, J. P. D., Brune, W. H., Ng, N. L., Wright, J. P., Croasdale, D. R., Worsnop, D. R., Davidovits, P., and Onasch, T. B.: Characterization of aerosol photooxidation flow reactors: heterogeneous oxidation, secondary organic aerosol formation and cloud condensation nuclei activity measurements, Atmos. Meas. Tech., 4, 445–461, https://doi.org/10.5194/amt-4-445-2011, 2011.

Lambe, A. T., Chhabra, P. S., Onasch, T. B., Brune, W. H., Hunter, J. F., Kroll, J. H., Cummings, M. J., Brogan, J. F., Parmar, Y., Worsnop, D. R., Kolb, C. E., and Davidovits, P.: Effect of oxidant concentration, exposure time, and seed particles on secondary organic aerosol chemical composition and yield, Atmos. Chem. Phys., 15, 3063–3075, https://doi.org/10.5194/acp-15-3063-2015, 2015.

Lambe, A., Massoli, P., Zhang, X., Canagaratna, M., Nowak, J., Daube, C., Yan, C., Nie, W., Onasch, T., Jayne, J., Kolb, C., Davidovits, P., Worsnop, D., and Brune, W.: Controlled nitric

oxide production via $O(^1D) + N_2O$ reactions for use in oxidation flow reactor studies, Atmos. Meas. Tech., 10, 2283–2298, https://doi.org/10.5194/amt-10-2283-2017, 2017.

Lambe, A. T., Krechmer, J. E., Peng, Z., Casar, J. R., Carrasquillo, A. J., Raff, J. D., Jimenez, J. L., and Worsnop, D. R.: HO_x and NO_x production in oxidation flow reactors via photolysis of isopropyl nitrite, isopropyl nitrite-d_7, and 1, 3-propyl dinitrite at $\lambda = 254$, 350, and 369 nm, Atmos. Meas. Tech., 12, 299–311, https://doi.org/10.5194/amt-12-299-2019, 2019.

Langridge, J. M., Ball, S. M., Shillings, A. J. L., and Jones, R. L.: A broadband absorption spectrometer using light emitting diodes for ultrasensitive, in situ trace gas detection, Rev. Sci., 79, 123110, https://doi.org/10.1063/1.3046282, 2008.

Lee, B. H., Lopez-Hilfiker, F. D., Mohr, C., Kurten, T., Worsnop, D. R., and Thornton, J. A.: An Iodide-Adduct High-Resolution Time-of-Flight Chemical-Ionization Mass Spectrometer: Application to Atmospheric Inorganic and Organic Compounds, Environ. Sci. Technol., 48, 6309–6317, 2014.

Li, R., Palm, B. B., Ortega, A. M., Hlywiak, J., Hu, W., Peng, Z., Day, D. A., Knote, C., Brune, W. H., De Gouw, J. A., and Jimenez, J. L.: Modeling the Radical Chemistry in an Oxidation Flow Reactor: Radical Formation and Recycling, Sensitivities, and the OH Exposure Estimation Equation, J. Phys. Chem. A, 119, 4418–4432, https://doi.org/10.1021/jp509534k, 2015.

Manion, J. A., Huie, R. E., Levin, R. D., Burgess Jr., D. R., Orkin, V. L., Tsang, W., McGivern, W. S., Hudgens, J. W., Knyazev, V. D., Atkinson, D. B., Chai, E., Tereza, A. M., Lin, C.-Y., Allison, T. C., Mallard, W. G., Westley, F., Herron, J. T., Hampson, R. F., and Frizzell, D. H.: NIST Chemical Kinetics Database, NIST Standard Reference Database 17, Version 7.0 (Web Version), Release 1.6.8, Data version 2015.09, National Institute of Standards and Technology, Gaithersburg, Maryland, 20899-8320, available at: http://kinetics.nist.gov/ (last access: 13 May 2020), 2015.

Melaas, E. K., Wang, J. A., Miller, D. L., and Friedl, M. A.: Interactions between urban vegetation and surface urban heat islands: a case study in the Boston metropolitan region, Environ. Res. Lett., 11, 054020, https://doi.org/10.1088/1748-9326/11/5/054020, 2016.

Middlebrook, A. M., Bahreini, R., Jimenez, J. L., and Canagaratna, M. R.: Evaluation of Composition-Dependent Collection Efficiencies for the Aerodyne Aerosol Mass Spectrometer using Field Data, Aerosol. Sci. Technol., 46, 258–271, 2012.

Nah, T., Sanchez, J., Boyd, C. M., and Ng, N. L.: Photochemical Aging of α-pinene and β-pinene Secondary Organic Aerosol formed from Nitrate Radical Oxidation, Environ. Sci. Technol., 50, 222–231, https://doi.org/10.1021/acs.est.5b04594, 2016.

Ng, N. L., Brown, S. S., Archibald, A. T., Atlas, E., Cohen, R. C., Crowley, J. N., Day, D. A., Donahue, N. M., Fry, J. L., Fuchs, H., Griffin, R. J., Guzman, M. I., Herrmann, H., Hodzic, A., Iinuma, Y., Jimenez, J. L., Kiendler-Scharr, A., Lee, B. H., Luecken, D. J., Mao, J., McLaren, R., Mutzel, A., Osthoff, H. D., Ouyang, B., Picquet-Varrault, B., Platt, U., Pye, H. O. T., Rudich, Y., Schwantes, R. H., Shiraiwa, M., Stutz, J., Thornton, J. A., Tilgner, A., Williams, B. J., and Zaveri, R. A.: Nitrate radicals and biogenic volatile organic compounds: oxidation, mechanisms, and organic aerosol, Atmos. Chem. Phys., 17, 2103–2162, https://doi.org/10.5194/acp-17-2103-2017, 2017.

Orlando, J. J. and Tyndall, G. S.: Laboratory studies of organic peroxy radical chemistry: an overview with emphasis on recent issues of atmospheric significance, Chem. Soc. Rev., 41, 6294–6317, https://doi.org/10.1039/C2CS35166H, 2012.

Orphal, J., Fellows, C. E., and Flaud, P.-M.: The visible absorption spectrum of NO_3 measured by high-resolution Fourier transform spectroscopy, J. Geophys. Res.-Atmos., 108, 4077, https://doi.org/10.1029/2002JD002489, 2003.

Palm, B. B., Campuzano-Jost, P., Day, D. A., Ortega, A. M., Fry, J. L., Brown, S. S., Zarzana, K. J., Dube, W., Wagner, N. L., Draper, D. C., Kaser, L., Jud, W., Karl, T., Hansel, A., Gutiérrez-Montes, C., and Jimenez, J. L.: Secondary organic aerosol formation from in situ OH, O_3, and NO_3 oxidation of ambient forest air in an oxidation flow reactor, Atmos. Chem. Phys., 17, 5331–5354, https://doi.org/10.5194/acp-17-5331-2017, 2017.

Peng, Z. and Jimenez, J. L.: Modeling of the chemistry in oxidation flow reactors with high initial NO, Atmos. Chem. Phys., 17, 11991–12010, https://doi.org/10.5194/acp-17-11991-2017, 2017.

Peng, Z. and Jimenez, J. L.: KinSim: A Research-Grade, User-Friendly, Visual Kinetics Simulator for Chemical-Kinetics and Environmental-Chemistry Teaching, J. Chem. Educ., 96, 806–811, https://doi.org/10.1021/acs.jchemed.9b00033, 2019.

Peng, Z. and Jimenez, J.: Downloadable KinSim cases and mechanisms, available at: https://tinyurl.com/kinsim-cases#bookmark=kix.6zu8zdwq2lce, last access: 13 May 2020.

Peng, Z., Day, D. A., Stark, H., Li, R., Lee-Taylor, J., Palm, B. B., Brune, W. H., and Jimenez, J. L.: HO_x radical chemistry in oxidation flow reactors with low-pressure mercury lamps systematically examined by modeling, Atmos. Meas. Tech., 8, 4863–4890, https://doi.org/10.5194/amt-8-4863-2015, 2015.

Peng, Z., Palm, B. B., Day, D. A., Talukdar, R. K., Hu, W., Lambe, A. T., Brune, W. H., and Jimenez, J. L.: Model Evaluation of New Techniques for Maintaining High-NO Conditions in Oxidation Flow Reactors for the Study of OH-Initiated Atmospheric Chemistry, ACS Earth Space Chem., 2, 72–86, https://doi.org/10.1021/acsearthspacechem.7b00070, 2018.

Peng, Z., Lee-Taylor, J., Orlando, J. J., Tyndall, G. S., and Jimenez, J. L.: Organic peroxy radical chemistry in oxidation flow reactors and environmental chambers and their atmospheric relevance, Atmos. Chem. Phys., 19, 813–834, https://doi.org/10.5194/acp-19-813-2019, 2019.

Platz, J., Nielsen, O. J., Wallington, T. J., Ball, J. C., Hurley, M. D., Straccia, A. M., Schneider, W. F., and Sehested, J.: Atmospheric Chemistry of the Phenoxy Radical, C_6H_5O: UV Spectrum and Kinetics of its Reaction with NO, NO_2 and O_2, J. Phys. Chem. A, 102, 7964–7974, https://doi.org/10.1021/jp982221l, 1998.

Rudich, Y., Talukdar, R. K., Imamura, T., Fox, R. W., and Ravishankara, A. R.: Uptake of NO_3 on KI solutions: rate coefficient for the $NO_3 + I$-reaction and gas-phase diffusion coefficients for NO_3, Chem. Phys. Lett., 261, 467–473, 1996.

Saunders, S. M., Jenkin, M. E., Derwent, R. G., and Pilling, M. J.: Protocol for the development of the Master Chemical Mechanism, MCM v3 (Part A): tropospheric degradation of non-aromatic volatile organic compounds, Atmos. Chem. Phys., 3, 161–180, https://doi.org/10.5194/acp-3-161-2003, 2003.

Short, K. C.: Spatial wildfire occurrence data for the United States, 1992–2015, 4th Edition, https://doi.org/10.2737/RDS-2013-0009.4, 2017.

Stutz, J., Alicke, B., Ackermann, R., Geyer, A., White, A., and Williams, E.: Vertical profiles of NO_3, N_2O_5, O_3, and NO_x

in the nocturnal boundary layer: 1. Observations during the Texas Air Quality Study 2000, J. Geophys. Res., 109, D12306, https://doi.org/10.1029/2003jd004209, 2004.

Vandaele, A. C., Hermans, C., Simon, P. C., Carleer, M., Colin, R., Fally, S., Mérienne, M. F., Jenouvrier, A., and Coquart, B.: Measurements of the NO_2 absorption cross-section from 42 000 cm^{-1} to 10 000 cm^{-1} (238–1000 nm) at 220 K and 294 K., J. Quant. Spectrosc. Radiat. Transf., 59, 171–184, https://doi.org/10.1016/S0022-4073(97)00168-4, 1998.

Venables, D. S., Gherman, T., Orphal, J., Wenger, J. C., and Ruth, A. A.: High Sensitivity in Situ Monitoring of NO_3 in an Atmospheric Simulation Chamber Using Incoherent Broadband Cavity-Enhanced Absorption Spectroscopy, Environ. Sci. Technol., 40, 6758–6763, https://doi.org/10.1021/es061076j, 2006.

Voigt, S., Orphal, J., Bogumil, K., and Burrows, J. P.: The temperature dependence (203–293 K) of the absorption cross sections of O_3 in the 230–850 nm region measured by Fourier-transform spectroscopy, J. Photoch. Photobio. A, 143, 1–9, 2001.

Wagner, C., Hanisch, F., Holmes, N., de Coninck, H., Schuster, G., and Crowley, J. N.: The interaction of N_2O_5 with mineral dust: aerosol flow tube and Knudsen reactor studies, Atmos. Chem. Phys., 8, 91–109, https://doi.org/10.5194/acp-8-91-2008, 2008.

Warneck, P. and Williams, J.: The Atmospheric Chemist's Companion, Springer, Dordrecht, https://doi.org/10.1007/978-94-007-2275-0, 2012.

Wayne, R. P., Barnes, I., Biggs, P., Burrows, J. P., Canosa-Mas, C. E., Hjorth, J., Le Bras, G., Moortgat, G. K., Perner, D., Poulet, G., Restelli, G., and Sidebottom, H.: The nitrate radical: physics, chemistry, and the atmosphere, Atmos. Environ. A, 25, 1–203, 1991.

Wood, E. C., Wooldridge, P. J., Freese, J. H., Albrecht, T., and Cohen, R. C.: Prototype for In Situ Detection of Atmospheric NO_3 and N_2O_5 via Laser-Induced Fluorescence, Environ. Sci. Technol., 37, 5732–5738, https://doi.org/10.1021/es034507w, 2003.

Xu, W., Lambe, A., Silva, P., Hu, W., Onasch, T., Williams, L., Croteau, P., Zhang, X., Renbaum-Wolff, L., Fortner, E., Jimenez, J. L., Jayne, J., Worsnop, D., and Canagaratna, M.: Laboratory evaluation of species-dependent relative ionization efficiencies in the Aerodyne Aerosol Mass Spectrometer, Aerosol. Sci. Technol., 52, 626–641, https://doi.org/10.1080/02786826.2018.1439570, 2018.